



Cite this: *RSC Adv.*, 2024, **14**, 22781

## Structure–activity relationships, product species distribution and the mechanism of effect of multi-component flue gas on $\text{Hg}^0$ adsorption and oxidation over $\text{CuO/ACs}^\dagger$

Li Tong,<sup>†,a</sup> Penglai Zuo,<sup>†,a</sup> Xiaoxi Zhang,<sup>a</sup> Quanming Liang,<sup>a</sup> Kun Wang,<sup>a</sup> Yawen Yang,<sup>a</sup> Jieyu Liu,<sup>a</sup> Haixin Guo<sup>ID, \*b</sup> and Peng Zhang<sup>\*c</sup>

A series of Cu-doped activated cokes ( $\text{CuO/ACs}$ ) were synthesized *via* an impregnation method and applied for the removal of elemental mercury ( $\text{Hg}^0$ ). Structure–activity relationships between  $\text{Hg}^0$  removal and  $\text{CuO/AC}$  surface characteristics were identified.  $\text{Hg}^0$  removal over  $\text{CuO/AC}$  occurs through a combination of physisorption and chemisorption and is mainly dominated by chemisorption. It was found that 1 nm micropores facilitate  $\text{Hg}^0$  physisorption.  $\text{Hg}^0$  could weakly adsorb onto an O-terminated crystal layer, whereas strongly adsorb onto Cu-terminated single highly dispersed, clustered and bulk  $\text{CuO}$  (110) crystal planes *via* the Mars–Maessen mechanism. Product distributions and mechanisms of  $\text{Hg}^0$  adsorption and oxidation over the  $\text{CuO/AC}$  catalyst under multi-component flue gases are also discussed.  $\text{O}_2$  enhances both physisorption and chemisorption toward  $\text{Hg}^0$  by 38%. Inhibition of  $\text{Hg}^0$  removal by  $\text{SO}_2$  originates from the competitive adsorption and deactivation of CuO cation vacancies, whereas the impact is weakened by  $\text{O}_2$  through generating 20% of physically adsorbed mercury product species. NO and  $\text{O}_2$  promote  $\text{Hg}^0$  chemisorption efficiency by 93% to form  $\text{Hg}(\text{NO}_3)_2$ . HOCl and/or  $\text{Cl}_2$  produced by HCl can oxidize 100% of  $\text{Hg}^0$  to  $\text{HgCl}_2$ , and the catalytic oxidation efficiency is approximately 29%, but  $\text{O}_2$  slightly lowers the  $\text{Hg}^0$  catalytic oxidation efficiency by 8%. The affinity ability between various flue gases and  $\text{Hg}^0$  follows the order  $\text{O}_2 < \text{NO} < \text{HCl}$ .

Received 2nd April 2024  
Accepted 4th July 2024

DOI: 10.1039/d4ra02483d  
[rsc.li/rsc-advances](http://rsc.li/rsc-advances)

### 1. Introduction

Mercury derived from fuel combustion has aroused wide concern owing to its unique chemical properties and has adverse effects on human health.<sup>1</sup> Among the various mercury species, elemental mercury ( $\text{Hg}^0$ ) is the hardest to capture using currently available pollution control devices.<sup>2,3</sup>

Numerous efforts have been undertaken for mercury removal by means of adsorption and oxidation, which proved to be helpful for controlling  $\text{Hg}^0$ .<sup>4–7</sup> To date, wet flue gas desulfurization (WFGD) has been regarded as an effective way for disposing  $\text{SO}_2$  and is adopted to remove  $\text{Hg}^{2+}$  after the oxidation of  $\text{Hg}^0$  in industry. However, the re-emission of mercury during

the WFGD progress is a serious problem. Activated carbon injection (ACI) has been recognized as the mainly commercialized technology to remove mercury in the commercial application of coal-fired power plants, especially for activated carbons impregnated with halogen.<sup>8</sup> However, several shortcomings, such as carbon consumption, larger occupied area and higher costs, hamper its practical applications. In recent years, the use of transition metal oxides as oxidants for heterogeneous  $\text{Hg}^0$  removal has been a growing field.<sup>9,10</sup> Nevertheless, it is difficult to remodel the existing flue gas flow control devices, and catalysts' mechanical strength should be high enough to avoid dust erosion. For this purpose, materials could be employed downstream from fabric filters or electrostatic precipitators where temperature is commonly less than 160 °C.<sup>8</sup>

Among the various low-cost transition metal catalysts, copper oxides have been most developed because of their high activity for multi-pollutants, such as  $\text{SO}_2$ , NO and VOCs.<sup>11–13</sup> However, pure  $\text{CuO}$  is almost inert to  $\text{Hg}^0$  removal. Therefore, Cu-based catalysts were employed to enhance  $\text{Hg}^0$  removal performance (see Table S1 in the ESI<sup>†</sup>).<sup>14–16</sup> For example, Zhang *et al.*<sup>14</sup> studied  $\text{Hg}^0$  adsorption over novel copper-based porous metal-organic

<sup>a</sup>Institute of Urban Safety and Environmental Science, Beijing Academy of Science and Technology, Beijing 100054, China

<sup>b</sup>Agro-Environmental Protection Institute, Ministry of Agriculture and Rural Affairs, Tianjin 300191, China. E-mail: [haixin\\_g@126.com](mailto:haixin_g@126.com)

<sup>c</sup>National Center for Occupational Safety and Health, National Health Commission of the People's Republic of China, Beijing 102308, China. E-mail: [zhangpengbd@163.com](mailto:zhangpengbd@163.com)

† Electronic supplementary information (ESI) available. See DOI: <https://doi.org/10.1039/d4ra02483d>

‡ Co-first author: Li Tong and Penglai Zuo contributed equally to this work.



frameworks (Cu-MOFs) with a chlorine-rich functional group and found that the resulting adsorbent had an  $\text{Hg}^0$  removal efficiency of 91.8% at 120 °C in an  $\text{N}_2$  atmosphere. Liu *et al.*<sup>15</sup> indicated that  $\text{CuO/g-C}_3\text{N}_4$  materials had the  $\text{Hg}^0$  removal efficiency exceeding 98.0% at 120 °C in an  $\text{N}_2$  atmosphere. As a result, the  $\text{Hg}^0$  removal performances over the Cu-based catalysts significantly vary in support. The active coke (AC), which is a common carbon-based material and has the characteristics of activated carbon, is typically considered a good candidate support for  $\text{Hg}^0$  removal at low temperatures due to the lower expense and excellent mechanical strength.<sup>17</sup> Zhao *et al.*<sup>16</sup> investigated the effects of various synthesis factors on  $\text{HNO}_3$  plus copper-modified ACs for  $\text{Hg}^0$  removal. Still, the crystal structure affecting the mercury removal performance has not been studied in detail. CuO supported on the AC as a material system for  $\text{Hg}^0$  removal had ever been demonstrated to be active for  $\text{Hg}^0$  removal by fewer researchers, but little attention had been paid to the occurrence state and shape of the copper element and the detailed bonding sites for  $\text{Hg}^0$  to reveal the structure–activity relationship between  $\text{Hg}^0$  removal performance and CuO/AC surface characteristics.

Actually, the pollutants' removal performance is a result of the interaction among pollutants, materials, and the co-existing flue gas. In particular,  $\text{Hg}^0$  is inferior in the gas volume and dipole moment, thus the removal performance is not mass transfer favored under the multi-component flue gas. Therefore, the  $\text{Hg}^0$  removal selectivity strongly depends on the reciprocal effect of the material structures and flue gas components. The flue gas composition is primarily determined by the coal matrix and significantly affects the  $\text{Hg}^0$  removal efficiency, particularly for  $\text{O}_2$ ,  $\text{SO}_2$ , NO, and HCl. Laboratory experiments indicated that  $\text{O}_2$  or HCl showed enhancement in  $\text{Hg}^0$  oxidation.<sup>18,19</sup> However, the impact of NO or  $\text{SO}_2$  on  $\text{Hg}^0$  removal has not reached a consensus,<sup>19–21</sup> which mainly depends on the synthetic effect of competitive adsorption, poisoning and the newly generated active groups responsible for  $\text{Hg}^0$  removal. However, the information on the internal reaction mechanism of  $\text{Hg}^0$  and multi-component flue gases over CuO/AC was still insufficient for Cu-based AC catalysts.

Based on the above-mentioned statement, this work focuses on building the structure–activity relationship between  $\text{Hg}^0$  removal performance and CuO/AC surface characteristics, and investigates the effect of multi-component flue gas and product species distribution for  $\text{Hg}^0$  adsorption and oxidation over the CuO/AC. Furthermore, the affinity ability between different flue gases and  $\text{Hg}^0$  over the CuO/AC is discussed, and the probable reaction mechanisms are also proposed. In the present work, insights into the structure–activity relationships between the  $\text{Hg}^0$  removal performance and the CuO/AC provide guidance for the improvement of the current preparation method. Furthermore, exploring the reaction mechanism facilitates  $\text{Hg}^0$  removal through optimizing the proportion of flue gas components to enhance the  $\text{Hg}^0$  removal selectivity, and then probing into the product species distributions facilitates the regulation of the migration direction of product species, which oriently improve the adsorption efficiency or the catalytic oxidation efficiency instead of merely improving the material structure.

## 2. Experimental

### 2.1. Material preparation

The cylinder-shaped support with a diameter of 8 mm is a kind of commercial activated coke. The preparation procedure is as follows:

(1) Prior to use, virgin ACs were ground and crushed to 40–80 mesh. Afterwards, they were washed and rotated with distilled water and quickly dried at 110 °C for 14 h.

(2) Then, the CuO/ACs were synthesized by an equivalent-volume impregnation method with cupric nitrate as the precursor. The ACs were added into a solution with a required amount of cupric nitrate with the assistance of an ultrasonic cleaner for 0.5 h.

(3) Finally, the materials were dried at 110 °C for 14 h, followed by calcination under an Ar atmosphere at 300 °C for 3 h.

The catalyst is named M% CuO/AC, where M represents the mass ratio of copper oxide to AC.

### 2.2. Characterization

The samples' porosity characteristics were obtained using the nitrogen ( $\text{N}_2$ ) adsorption–desorption method (Autosorb iQ, Quantachrome). Before measurement, all the CuO/ACs were outgassed at 120 °C for 12 h. X-ray diffraction (XRD) measurements were carried out using a powder diffractometer (Rigaku D/Max-RA). An ESCALAB 250 X-ray photoelectron spectrometer equipped with a monochromatic Al  $\text{K}\alpha$  source was employed to determine the elemental chemical states of the materials. Temperature Programmed Reduction (TPR) profiles of the samples were collected using an ASAP ChemiSorb 2920.

The technique of temperature-programmed desorption coupled with a  $\text{Hg}^0$  analyzer ( $\text{Hg}^0$ -TPD) was used to analyze the adsorbed mercury product species and its amount on the catalysts. After the materials were placed in a  $\text{Hg}^0$ -containing gas flow for 2 h, the desorption process was recorded from 40 °C to 600 °C at a 10 °C min<sup>−1</sup> heating rate in  $\text{N}_2$ .

### 2.3. Activity test

The removal performances of the samples were evaluated using a quartz microreactor, and the experimental device is referenced to our previous research.<sup>20</sup> Approximately 50 mg catalysts were used in each test. The reaction temperature is modulated through a heating furnace outside. A sealed  $\text{Hg}^0$  permeation device was employed to provide a constant  $\text{Hg}^0$  concentration. To shorten the experimental time, a higher initial  $\text{Hg}^0$  concentration was chosen as  $270 \pm 5 \mu\text{g m}^{-3}$ . The Lumex RA-915M+  $\text{Hg}^0$  analyzer conventionally monitors the outlet  $\text{Hg}^0$  concentration. The simulated flue gases at a total flow rate of 300 mL min<sup>−1</sup>, consisting of NO, HCl,  $\text{SO}_2$  or  $\text{O}_2$ , balanced in  $\text{N}_2$  were accurately accommodated by the mass flowmeters. The weight hourly space velocity (WHSV) was calculated to be  $3.6 \times 10^5 \text{ mL g}^{-1} \text{ h}^{-1}$ . The pipeline was wrapped with heating tape to prevent  $\text{Hg}^0$  deposition by heating the pipe temperature to 80 °C. To ensure equal experimental conditions, the CuO/AC catalyst was purged with  $\text{N}_2$  for 20 min before each test. Moreover, a needle valve was added into the gaseous channel for the



determination of the initial  $\text{Hg}^0$  concentration to eliminate the pressure drop caused by adding the CuO/AC samples to the empty quartz microreactor. In this work, we defined three terms: total removal efficiency, adsorption efficiency and catalytic oxidation efficiency, which were calculated based on the 2 h experimental results; it therefore referred to the cumulative efficiency. The cumulative total removal efficiency ( $\eta_{\text{cap}}$ ) was calculated based on the difference in the integral area of inlet and outlet  $\text{Hg}^0$ , and the cumulative adsorption efficiency ( $\eta_{\text{ads}}$ ) was calculated on the basis of the integral area of the  $\text{Hg}^0$ -TPD curve after pre-adsorption in a mercury-containing flue gas for 2 h. Therefore, the cumulative catalytic oxidation efficiency ( $\eta_{\text{oxi}}$ ) is defined as  $(\eta_{\text{cap}}) - (\eta_{\text{ads}})$ . The breakthrough ratio of the samples is defined as follows:

$$\text{Breakthrough ratio} = \frac{C(\text{Hg}_{\text{outlet}}^0)}{C(\text{Hg}_{\text{inlet}}^0)} \times 100\% = \frac{C_{\text{out}}}{C_{\text{in}}} \quad (1)$$

where  $C(\text{Hg}_{\text{inlet}}^0)$  and  $C(\text{Hg}_{\text{outlet}}^0)$  denote the inlet and outlet  $\text{Hg}^0$  concentrations of the fixed bed, respectively.

### 3. Results and discussion

#### 3.1. Structure–activity relationship between the $\text{Hg}^0$ removal performance and the surface properties of CuO/AC

**3.1.1.  $\text{Hg}^0$  removal activity.** The metal oxide loading value affects not only the aggregation and dispersion of materials but also its crystal structure and valence states.<sup>22</sup> Accordingly, the impact of Cu loadings on the  $\text{Hg}^0$  removal was investigated. Fig. 1 illustrates the removal activity toward  $\text{Hg}^0$  over the CuO/ACs with different CuO loadings in a  $\text{N}_2$  atmosphere. It could be observed that the unmodified AC could hardly capture  $\text{Hg}^0$ , and there was also no removal of  $\text{Hg}^0$  over pure CuO (data are not shown), but the activities continued to improve with the CuO content increasing to 20%. The results indicate that an intense interaction appears between the AC support and the active metal oxide component during the  $\text{Hg}^0$  removal process. However, it was noted that the increment grew slightly when the Cu content ranged from 12% to 20%. Given both the cost and

the performance, the CuO loading values that appear in the following are set as 12%.

**3.1.2. Effect of reaction temperature.** Investigations on the reaction mechanism of 12% CuO/AC were performed as functions of temperature in the range of 60 °C to 180 °C with a constant gradient of 40 °C. As shown in Fig. 2, the activity toward  $\text{Hg}^0$  reduced with the ascension of the temperature ranging from 60 °C to 180 °C. Three genres of catalytic oxidation, physisorption, and chemisorption can be defined to differentiate the removal mechanisms over various materials. Physisorption theory presumes that gaseous pollutants are preferential to diffuse to the material surfaces at lower temperature. The clear suppression in  $\text{Hg}^0$  removal with the increase in temperature demonstrates that physisorption takes effect in the  $\text{Hg}^0$  removal process over the 12% CuO/AC.

**3.1.3. Effect of the physical property of CuO/ACs on the  $\text{Hg}^0$  removal.** To further identify the scope of physisorption, the  $\text{N}_2$  adsorption–desorption isotherms and pore size distributions of CuO/ACs were recorded (see Fig. S1 in the ESI†), and merely part of the data are depicted in Fig. 3 to avoid the results indistinctly displayed. As can be seen, all the isotherms were indicative of a typical IV type with H4 hysteresis loops according to the IUPAC classification,<sup>23</sup> which suggests the presence of a mixture of narrow slit-like micropores and mesopores with irregular structures. Most pore sizes of all the catalysts were less than 2 nm. It should be noted that, after modification, an increase in CuO loadings to 12% enhanced the proportion for micropores distributing on 1 nm, but a further increase in the CuO content decreased the proportion. Therefore, it can be deduced that micropores centered at 1 nm may be a critical factor in determining the almost identical performance for 12% CuO/AC compared to that of catalysts with higher loadings. Table 1 summarizes the calculated structure parameters of AC with different CuO contents. It could be observed that AC support possessed the largest surface area and the well-developed porous fabric. However, the surface area and total pore volume followed a descending order as the CuO content increased. This appearance might occur on account of the fact

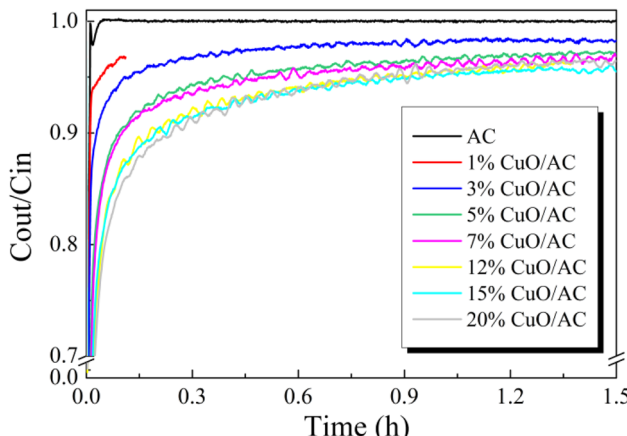


Fig. 1 Breakthrough curves of  $\text{Hg}^0$  over virgin AC and CuO/AC with different CuO contents balanced in a pure  $\text{N}_2$  atmosphere at 120 °C.

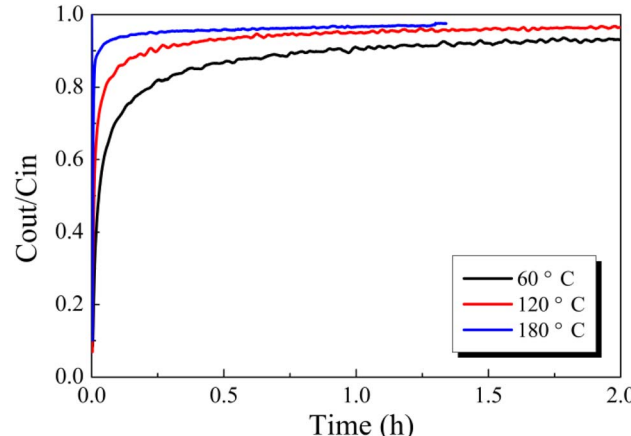


Fig. 2 Effect of reaction temperature on  $\text{Hg}^0$  removal over 12% CuO/AC under a pure  $\text{N}_2$  atmosphere.



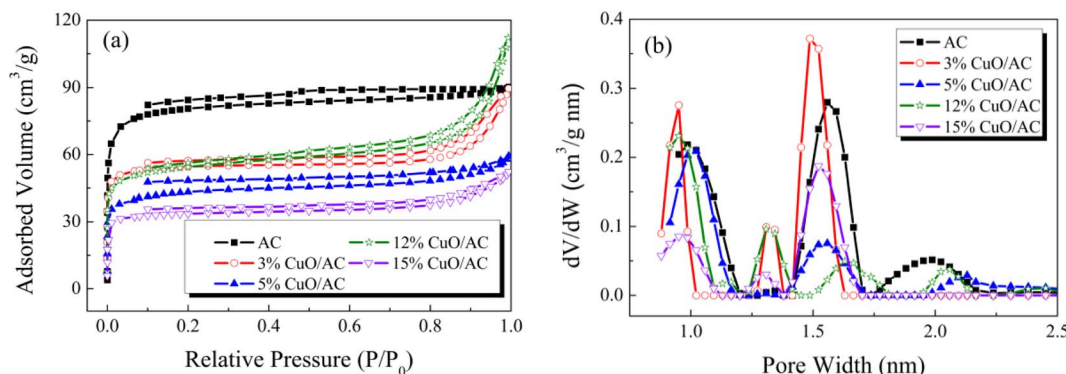


Fig. 3 (a) N<sub>2</sub> adsorption–desorption isotherms and (b) pore size distribution of the catalysts with different CuO contents.

Table 1 Structural parameters of CuO/AC with different CuO contents<sup>a</sup>

Samples	BET surface area (m <sup>2</sup> g <sup>-1</sup> )	Total pore volume (cm <sup>3</sup> g <sup>-1</sup> )	Average pore diameter (nm)
AC	251	0.138	2.20
1% CuO/AC	246	0.123	2.20
3% CuO/AC	193	0.131	2.72
5% CuO/AC	191	0.109	2.29
7% CuO/AC	160	0.102	2.71
12% CuO/AC	138	0.090	2.59
15% CuO/AC	121	0.077	2.56
20% CuO/AC	93	0.070	2.99

<sup>a</sup> The BET surface area was calculated from the N<sub>2</sub> adsorption isotherms using the BET equation. The total pore volume was accessed from the amount of N<sub>2</sub> adsorbed at  $p/p_0 = 0.99$ . The average pore diameter was calculated based on four times the total pore volume divided by the specific surface area.

that CuO blocks into the pore channel of samples to cluster metal oxides augmented.<sup>1</sup> When the loading surpasses 12%, slit-like pores distributed on 1 nm are increasingly lessened.

Therefore, based on the comprehensive analysis above, it could be deduced that physisorption facilitates the Hg<sup>0</sup> removal but is not the only factor.

**3.1.4. XRD analysis.** As discussed, the removal mechanism toward Hg<sup>0</sup> is not solely dominated by physisorption. Thus, the chemical properties may be another governing factor for the performance of CuO/ACs. To reveal the occurrence state of the active species and corresponding crystal phases responsible for the Hg<sup>0</sup> activity, the XRD measurements of the CuO/ACs were carried out, as shown in Fig. 4. All reflections provided two typical diffraction peaks for the carbon matrix of AC support, which distributed on 26.78° and 43.38° (PDF# 89-8493), respectively, while the peaks at 25.65° and 36.60° (PDF# 82-1557) are attributed to SiO<sub>2</sub>. With the introduction of metal oxides and carbon matrixes, SiO<sub>2</sub> peaks were still clearly observed; although all these peaks were less intense, this suggests that the crystallites of virgin AC have not changed because of the modification of metal oxides. In addition, new diffraction peaks at 35.58°, 38.99°, 48.77°, 53.90°, 58.52°, 61.61° and 68.28° (PDF# 80-1916) emerged and are matched to copper

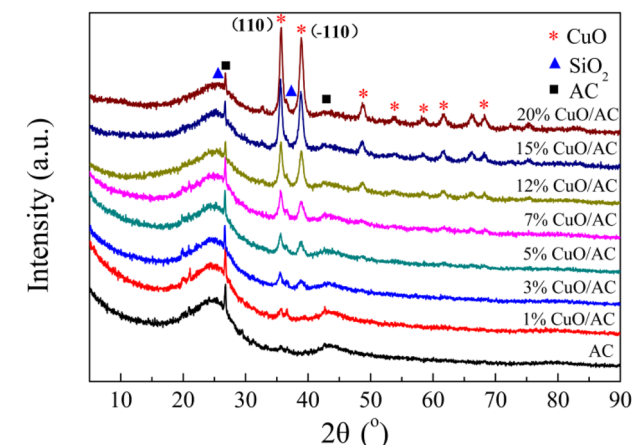


Fig. 4 X-ray diffraction patterns of CuO/AC catalysts with different CuO contents.

oxide,<sup>24,25</sup> which therein (110) and (−110) crystal planes oriented preponderate. The diffraction peaks of the other phases were not detected. The result indicates that copper existed in the form of CuO phase for the CuO/ACs catalysts when calcinated at 300 °C. Furthermore, doping metal oxides to AC shifted the diffraction peaks to a larger angle, implying that the CuO crystalline domains (shown in Table S2†) gradually grow according to the Scherrer formula,<sup>26,27</sup> which is likely related to the structural distortion of materials. As CuO contents ascend, the crystallinity of the active species becomes perfect, and that of grain diameters becomes bigger than the pores of the AC. Afterward, the CuO crystal particles deposit onto the surface of the AC and block the pores, which agrees with the BET analysis. The stacked CuO/AC catalysts probably further contribute to the nonuniform dispersion.

**3.1.5. H<sub>2</sub>-TPR analysis.** Redox behaviors of the CuO/ACs were analyzed by H<sub>2</sub>-TPR to further understand the enhancement effect of the AC modified by CuO active species for Hg<sup>0</sup> removal. As illustrated in Fig. 5, the virgin AC only exhibited one reduction peak located in 612 °C. This obvious peak is associated with the gasification of the AC support<sup>28</sup> and is also observed in 12% CuO/AC catalyst. After copper was added onto



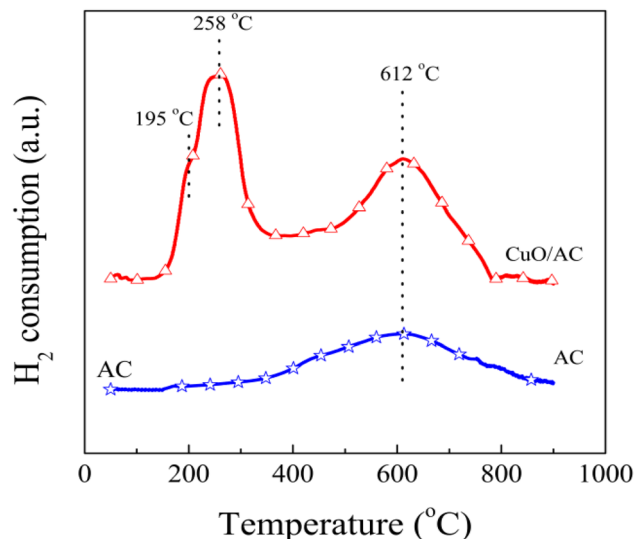


Fig. 5  $\text{H}_2$ -TPR profiles of virgin AC and the 12% CuO/AC catalyst.

AC, another reduction peak appeared at 258 °C with a shoulder reduction peak at roughly 195 °C.

The environment of the copper ions and/or their structures is quite complicated and can be classified into two types of form:  $\text{Cu}^{2+}$ , including the isolated form (highly-dispersed) and clustered form (bulk-like), as well as  $\text{Cu}^+$ . However, the two peaks could not be explained through the step-wise reductions of the supported copper species, such as  $\text{Cu}^{2+} \rightarrow \text{Cu}^+$  and  $\text{Cu}^+ \rightarrow \text{Cu}^0$ , because the areas for each peak are apparently distinct, and the reduction of  $\text{Cu}^+$  usually appears at high temperatures.<sup>29</sup> Moreover, many researchers<sup>29,30</sup> confirmed that most reduction of CuO occurred in a representative two-stage pattern at lower temperatures, where all the crystalline-supported  $\text{Cu}^{2+}$  ions reduce. Therefore, it can be concluded that the peak in the overlapped TPR profiles at 195 °C is associated with the reduction of the small two- and/or three-dimensional bulk CuO, weak magnetic associates, and isolated  $\text{Cu}^{2+}$  ions, whereas the peak centered at 258 °C corresponds to the reduction of large three-dimensional clusters of CuO and/or the bulk CuO phase. The lowering of reduction temperature evidences the redox ability of the supported copper oxide, which is greatly improved after modification. This is because the couple of  $\text{Cu}/\text{Cu}^+$  facilitates the reduction of the energy required for electron transport and/or boosts the mobility of the active oxygen, thus promoting the reactant activation and/or generation of surface oxygen vacancies.<sup>31,32</sup> The surface oxygen vacancies further result in structural distortion, which is in accordance with the XRD results.

**3.1.6. XPS analysis.** The structure-activity relationships between CuO/ACs and the  $\text{Hg}^0$  removal performance were further identified by analyzing the elemental chemical states and compositions before and after the reaction using XPS. The representative photoelectron profiles of O 1s, Cu 2p, and Hg 4f attaching to virgin and spent CuO/ACs are shown in Fig. 6. As depicted in Fig. 6(a), the O 1s profiles for virgin CuO/AC and spent CuO/AC samples were deconvoluted into three groups of

peaks. The sub-bands at a lower binding energy corresponded to the lattice oxygen ( $\text{O}_\alpha$ ). The two sub-bands at a higher binding energy were ascribed to chemisorbed oxygen, weakly bonded oxygen or oxygen vacancies ( $\text{O}_\beta$ ), and adsorbed water species or hydroxyl groups ( $\text{O}_\gamma$ ).<sup>31</sup> The proportion of each branch of O 1s over the sample surface was obtained by calculating the homologous peak area. It was noteworthy that no obvious changes happened in the ratio of  $\text{O}_\alpha$  while the content of  $\text{O}_\beta$  decreased markedly from 79.70% to 61.27%; on the contrary, the ratio of  $\text{O}_\gamma$  demonstrated an upward tendency from 2.01% to 20.37% after reactions. This result indicates that almost no difference is observed in the behavior of  $\text{O}_\alpha$  after the reaction, whereas  $\text{O}_\beta$  seems highly reactive and has dramatically been consumed after the reaction. Generally, the adsorption reaction would boost the transformation of valence states of catalysts, whereas the catalytic oxidation reaction just displays the opposite. Therefore, regarding CuO/AC, we infer that  $\text{O}_\beta$  should be responsible for the redox reaction of mercury adsorption.

Fig. 6(b) presents the Cu 2p XPS spectra and their Gaussian fitting patterns of fresh and spent 12% CuO/AC samples. The Cu 2p profile was typically deconvoluted into four peaks, which could be assigned to  $\text{Cu} 2p_{3/2}$ ,  $\text{Cu} 2p_{1/2}$  and two satellite peaks. For the fresh 12% CuO/AC, the  $\text{Cu} 2p_{3/2}$ ,  $\text{Cu} 2p_{1/2}$  and two satellite peaks are the three primary characteristic peaks of  $\text{Cu}^{2+}$ ,<sup>33</sup> which echos the XRD and  $\text{H}_2$ -TPR results. However, after the adsorption of  $\text{Hg}^0$  onto the surface of CuO/AC, the  $\text{Cu} 2p_{3/2}$  peak divided into two valence states. The binding energy in the range of 934.6–935 eV indicates the presence of CuO, while that centered at 933.8 eV is close to the  $\text{Cu}_2\text{O}$  peak,<sup>25</sup> demonstrating that CuO participates in removal progress and sectional species transform to  $\text{Cu}_2\text{O}$  after reaction. However, this result cannot exclude the simultaneous possibility of an adsorption behavior and catalytic oxidation during the  $\text{Hg}^0$  removal.

The Hg 4f XPS profiles of the spent 12% CuO/AC are shown in Fig. 6(c). A single peak centered at 103.3 eV in fresh 12% CuO/AC was ascribed to Si 2p and in line with the XRD results. After the reaction, an intense peak at 104.4 eV corresponding to  $\text{Hg} 4f_{5/2}$  was attributed to  $\text{HgO}$ , and another small peak at 99.6 eV was assigned to  $\text{Hg}^0$ .<sup>33</sup> This result demonstrates that the mercury species over the spent CuO/ACs consists of  $\text{Hg}^0$  and  $\text{HgO}$ . Therefore, the results manifest that the Hg removal activities are restrained not only by the carbon texture, but also by the chemical properties, especially the lattice oxygen and chemisorbed oxygen groups.

### 3.2. Effect of multi-component gases and product species analysis

**3.2.1. Effect of  $\text{O}_2$ .** The  $\text{Hg}^0$  removal performances were evaluated at different  $\text{O}_2$  concentrations. As displayed in Fig. 7, the initial breakthrough ratio of  $\text{Hg}^0$  promptly decreased to approximately 0.9 under pure  $\text{N}_2$ . Without  $\text{O}_2$ , the  $\text{Hg}^0$  bonds with lattice oxygen to generate weakly bonded  $\text{MO}_{x-1}\text{O}\text{--Hg}$  species, physically adsorbs mercury species, and/or reacts with chemisorbed oxygen to form  $\text{HgO}$  through the Mars–Maessen mechanism.<sup>34</sup> Therefore, the decrease in CuO/AC activity is mainly because the surface oxygen is continually covered or



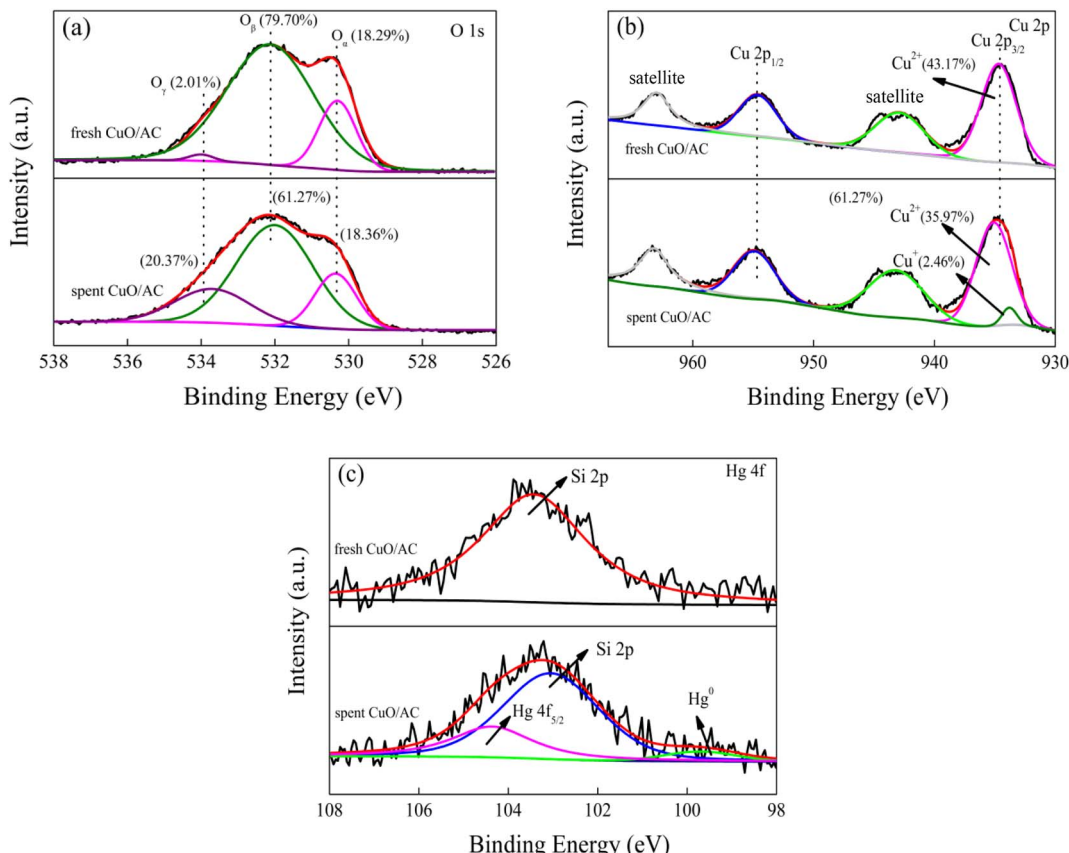


Fig. 6 (a) O 1s, (b) Cu 2p and (c) Hg 4f profiles of fresh AC and spent 12% CuO/AC catalysts.

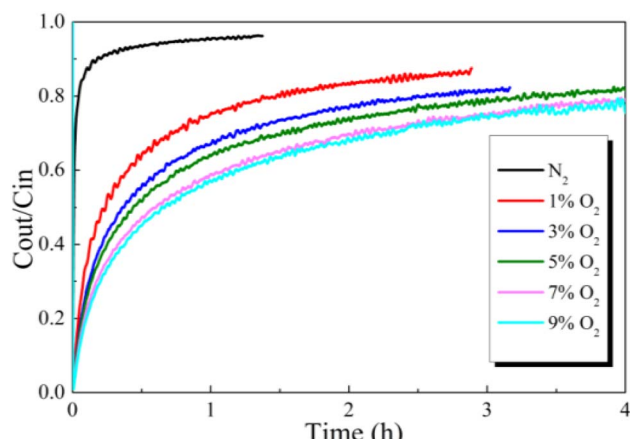


Fig. 7 Effect of O<sub>2</sub> concentration balanced in N<sub>2</sub> on Hg<sup>0</sup> removal over the 12% CuO/AC catalyst at 120 °C.

consumed. After a low level of O<sub>2</sub> flowed in, the Hg<sup>0</sup> removal rapidly increased, and improved step by step with the elevated O<sub>2</sub> content up to 9%. Nevertheless, no apparent increase was observed when the O<sub>2</sub> concentration surpassed 7%. Research by Li *et al.*<sup>19</sup> suggested that gas-phase O<sub>2</sub> could regenerate lattice oxygen or replenish chemisorbed oxygen over the catalysts, therefore exerting a promotional influence on Hg<sup>0</sup> removal. When the input O<sub>2</sub> achieves a specific content of 7%, gas-phase

oxygen and surface oxygen reach dynamic equilibrium over the 12% CuO/AC catalysts. Following that, the Hg<sup>0</sup> removal rate is almost of zeroth order with regard to the O<sub>2</sub> content. Thus, 7% is considered as the optimal O<sub>2</sub> concentration and will be used in the following experiments.

To reveal the reaction path toward Hg<sup>0</sup> removal under the O<sub>2</sub> atmosphere, the Hg<sup>0</sup>-TPD profiles were collected. As shown in Fig. 8, irrespective of the presence of O<sub>2</sub>, the Hg<sup>0</sup> decomposition peaks were in a similar position, beyond that the peak intensities were different. Therefore, it is inferred that the presence of O<sub>2</sub> will not alter the reaction path toward Hg<sup>0</sup> removal but will affect its removal efficiency. Two decomposition peaks appeared on the TPD spectra at around 144 °C and 178 °C. Nevertheless, after the samples were purged with N<sub>2</sub> for 1 h before the Hg<sup>0</sup>-TPD experiments, the desorption peak vanished at a lower temperature (shown in Fig. 8(b)). Therefore, the peak at 144 °C was assigned to the decomposition of the physically adsorbed mercury species when combined with XPS characterization results, while that peak centered at 178 °C was assigned to the HgO desorption. The Hg<sup>0</sup>-TPD profiles shown in Fig. 8(a) were further deconvoluted into two peaks based on the Gaussian method to distinguish the primary interaction mechanism, as shown in Fig. S2.<sup>†</sup> Interestingly, the area of HgO decomposition peak prevails regardless of the presence of O<sub>2</sub> in the pre-adsorption atmosphere, which suggests that chemisorption is the primary adsorption mechanism rather than physisorption.



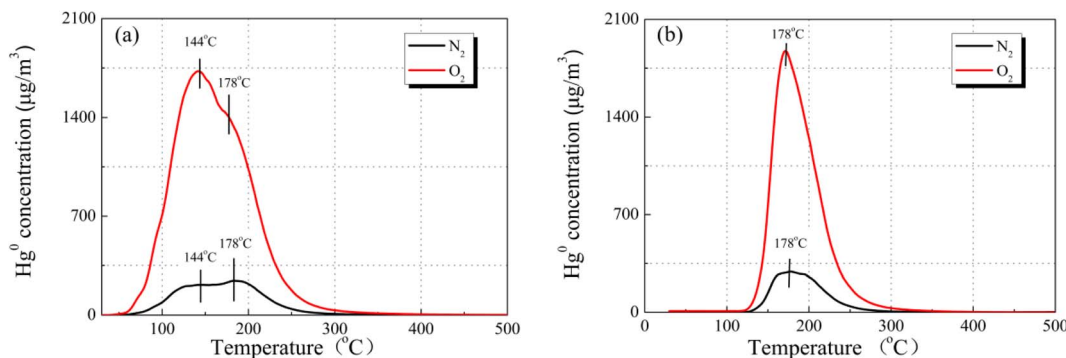


Fig. 8 Hg<sup>0</sup>-TPD patterns of the 12% CuO/AC catalyst after pre-adsorption in an N<sub>2</sub> or O<sub>2</sub> atmosphere (a) without N<sub>2</sub> purge and (b) with N<sub>2</sub> purge at 120 °C (pre-adsorption reaction conditions: 7% O<sub>2</sub> and N<sub>2</sub> as the balance).

Previously, Xiang *et al.*<sup>35</sup> have also carried out similar research for the Hg<sup>0</sup> adsorption mechanism on the CuO (110) crystal planes to evaluate the applicability of the SCR system for Hg<sup>0</sup> removal. In their research, they found that Hg<sup>0</sup> could strongly adsorb onto the Cu-terminated CuO (110) crystal planes, whereas weakly adsorb onto the O-terminated crystal layer, and the former bonding way was predicted to be the main adsorption mode. Accordingly, their conclusions are well consistent with our results obtained in this work.

**3.2.2. Effect of SO<sub>2</sub>.** The effects of various SO<sub>2</sub> atmospheres on the removal performance toward Hg<sup>0</sup> were investigated. As illuminated in Fig. 9(a), compared with the N<sub>2</sub> atmosphere, the addition of 200 ppm SO<sub>2</sub> significantly deteriorated the Hg<sup>0</sup> activity. An increase in the SO<sub>2</sub> concentration to 1000 ppm further marginally deteriorated the Hg<sup>0</sup> removal performance. A similar trend was also observed for the Hg<sup>0</sup> breakthrough curves by the addition of O<sub>2</sub>, as exhibited in Fig. 9(b), indicating that SO<sub>2</sub> still shows inhibition in Hg<sup>0</sup> removal even when it coexists with O<sub>2</sub>. However, the extent of the inhibitive effect is less intense with respect to that of the N<sub>2</sub> atmosphere. The SO<sub>2</sub> preponderates in the dipole moment and gas concentration, thus preventing Hg<sup>0</sup> collision onto the CuO/ACs surface through competitive adsorption. Furthermore, SO<sub>2</sub> exposed to metal oxides would react with active OH to generate metal

sulphate/sulphite, which destroys the surface cation vacancies of the metal oxides.<sup>36</sup> Despite in Section 3.2.1, it is proposed that adding O<sub>2</sub> could regenerate and/or replenish the active oxygen species, and the deterioration effect still cannot be eliminated. Accordingly, it is concluded that the consumption of reactive oxygen by the presence of SO<sub>2</sub> is not the essence for the decrease in Hg<sup>0</sup> removal performance because the O<sub>2</sub> content is ten times higher than that of SO<sub>2</sub>, manifesting that catalytic oxidation does not occur under an O<sub>2</sub> atmosphere.

Desorption experiments were conducted to understand the Hg<sup>0</sup> removal mechanism after pre-adsorption in SO<sub>2</sub>. As exhibited in Fig. 10, the Hg<sup>0</sup> decomposition peak appeared at approximately 142 °C. As previously reported,<sup>37</sup> the HgSO<sub>4</sub> desorption temperature was much higher than that of HgO. In comparison with the case of the O<sub>2</sub> atmosphere, we assume that the peak at 142 °C originates from the decomposition of physically adsorbed mercury species.

Therefore, it is demonstrated that the presence of O<sub>2</sub> weakens the suppression in physisorption toward Hg<sup>0</sup>, but the chemisorption is completely constrained by the presence of SO<sub>2</sub>. This result supports the above-mentioned viewpoint that the competitive adsorption between SO<sub>2</sub> and Hg<sup>0</sup> and the damage in the surface cation vacancies of the metal oxides take charge of the decrease in Hg<sup>0</sup> removal.

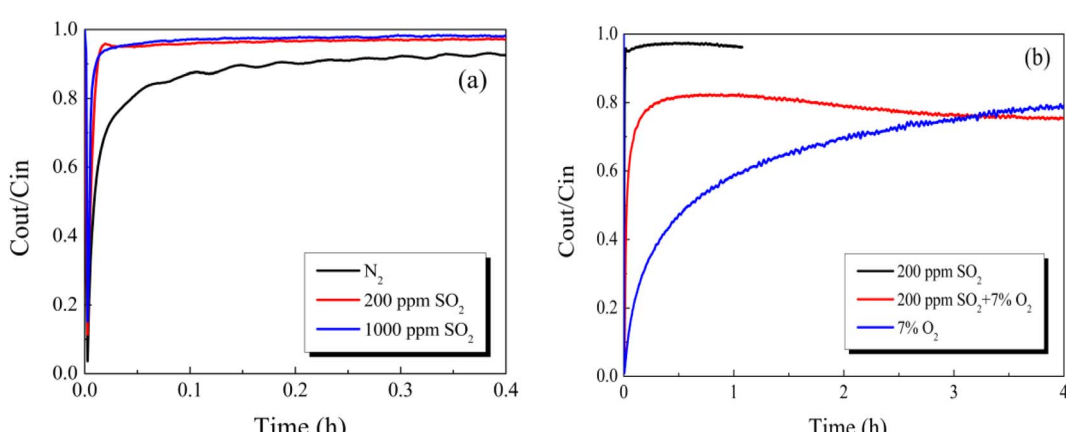


Fig. 9 Effect of SO<sub>2</sub> concentration balanced in an (a) N<sub>2</sub> or (b) O<sub>2</sub> atmosphere on Hg<sup>0</sup> removal over the 12% CuO/AC catalyst at 120 °C.

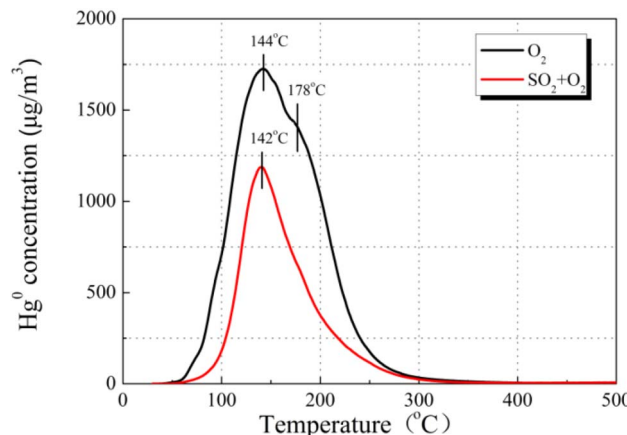


Fig. 10  $\text{Hg}^0$ -TPD patterns of the 12% CuO/AC catalyst after pre-adsorption in  $\text{SO}_2$  at 120 °C (pre-adsorption reaction conditions: 200 ppm of  $\text{SO}_2$ , 7%  $\text{O}_2$ , and  $\text{N}_2$  as the balance).

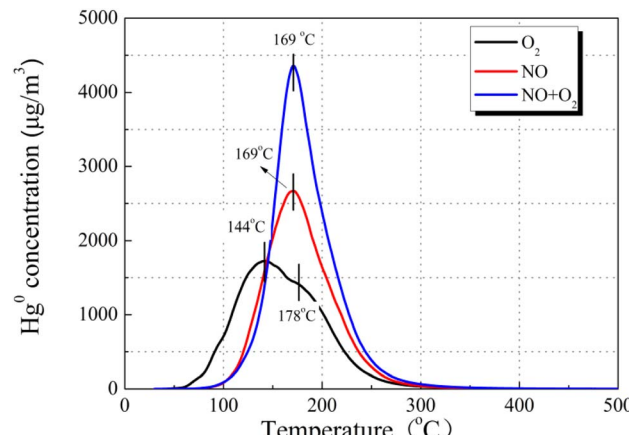


Fig. 12  $\text{Hg}^0$ -TPD patterns of the 12% CuO/AC catalyst after pre-adsorption in NO at 120 °C (pre-adsorption reaction conditions: 500 ppm of NO, 7%  $\text{O}_2$ , and  $\text{N}_2$  as the balance).

**3.2.3. Effect of NO.** Fig. 11 explores the  $\text{Hg}^0$  removal behaviors under different NO atmospheres over the CuO/AC catalyst at 120 °C. As observed, adding a low NO concentration of 100 ppm caused a rapid decrease in  $\text{Hg}^0$  breakthrough ratio, steadily dropping with the increase in NO concentration to 500 ppm. *In situ* DRIFT characterization indicated that NO can cohere onto the metal oxides to form  $\text{NO}_2$ ,  $\text{NO}^+$  and  $\text{NO}_3^-$ ,<sup>38</sup> and it is speculated that NO could occupy the C–O groups of activated coke/carbon surface to generate  $\text{NO}_2$  groups *via* chemisorption,<sup>39</sup> thereinto  $\text{NO}_2$  is an oxidant and can accept the outer electron of  $\text{Hg}^0$ , thereby promoting the oxidation. Moreover, researchers also affirmed that bidentate nitrate species might contribute to  $\text{Hg}^0$  removal.<sup>40</sup> However, further increasing the NO concentration resulted in an increase in the  $\text{Hg}^0$  breakthrough ratio. The NO could occupy the active sites for  $\text{Hg}^0$  adsorption due to a much higher concentration than that of  $\text{Hg}^0$ , resulting in slight inhibition in  $\text{Hg}^0$  removal. In addition, the  $\text{NO}_2$  is postulated to react with  $\text{Hg}^0$  to generate NO and  $\text{HgO}$ ,<sup>8</sup> then it is possible that NO at a higher concentration drives the reaction left, reducing the removal activity.

Breakthrough experiments of  $\text{Hg}^0$  over 12% CuO/AC were contrasted to identify the stimulative mechanisms for  $\text{Hg}^0$  activity in the presence of NO. As demonstrated in Fig. 11, introducing  $\text{O}_2$  into a NO atmosphere led to a prominent drop in the outlet  $\text{Hg}^0$  concentration compared with that of an individual NO or  $\text{O}_2$  atmosphere, indicating that the coexistence of  $\text{O}_2$  and NO plays a synergistic role in the removal of  $\text{Hg}^0$ . The formed  $\text{NO}_2$  species gradually increases after the  $\text{O}_2$ -containing gas was switched in, hence enhancing the  $\text{Hg}^0$  removal over the CuO/ACs. Furthermore, the  $\text{Hg}^0$  removal performance in NO obviously excels in that of  $\text{O}_2$ , which implies that the reaction paths for  $\text{Hg}^0$  removal under  $\text{O}_2$  and NO are different.

Accordingly, the  $\text{Hg}^0$ -TPD experiments were performed to clarify the mechanism after pre-adsorption in the presence of NO and  $\text{O}_2$ . As can be seen in Fig. 12, after pre-adsorption in the presence of NO, the positions of the primary  $\text{Hg}^0$  desorption peaks were basically identical irrespective of the presence of  $\text{O}_2$ , suggesting the same mercury product species, whose temperature is lower than that of  $\text{HgO}$  decomposition. Taking account of the flue gas components, the desorption peak center

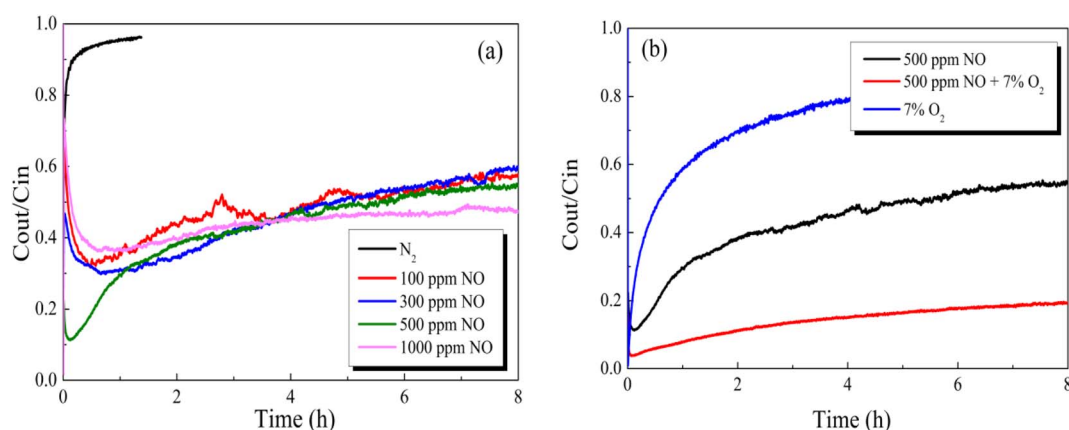


Fig. 11 Effect of NO concentration balanced in an (a)  $\text{N}_2$  or (b)  $\text{O}_2$  atmosphere on  $\text{Hg}^0$  removal over the 12% CuO/AC catalyst at 120 °C.



temperature merely possibly corresponds to  $\text{Hg}(\text{NO}_3)_2$  or  $\text{HgO}$ . Moreover, the  $\text{Hg}(\text{NO}_3)_2$  decomposition temperature was lower than that of  $\text{HgO}$ .<sup>41</sup> Hence, the stable product species toward  $\text{Hg}^0$  after pre-adsorption in NO is identified as  $\text{Hg}(\text{NO}_3)_2$ .

**3.2.4. Effect of HCl.** Further investigations on the effect of HCl on the removal performance toward  $\text{Hg}^0$  over CuO/ACs were conducted. As depicted in Fig. 13, when 1 ppm HCl flowed in, the outlet  $\text{Hg}^0$  concentration reduced gradually to zero after initially increasing and remained almost unchanged in the following 10 h. This appearance possibly stems from the initial active species such as atomic chlorine ( $\text{HOCl}$ )<sup>42</sup> insufficient to capture 100%  $\text{Hg}^0$ . As the newly formed HOCl species gradually accumulate, it increasingly promotes the  $\text{Hg}^0$  removal. Consequently, the HCl must first adsorb onto the material surface before reacting with the  $\text{Hg}^0$ . It is also suggested that  $\text{Cl}_2$  rather than HOCl can be produced to oxidize  $\text{Hg}^0$  through the Deacon reaction,<sup>43</sup> which might contribute to the  $\text{Hg}^0$  oxidation at lower temperatures. In addition, some researchers had indicated that the competitive adsorption reaction between HCl and  $\text{Hg}^0$  occurred *via* a partial Deacon reaction,<sup>11</sup> but this phenomenon could be eliminated in the present work because increasing the HCl concentration will sequentially accelerate the removal of  $\text{Hg}^0$  for the initial stages.

To better comprehend the nature of the interaction between HCl and  $\text{Hg}^0$ , we examined  $\text{Hg}^0$ -TPD patterns for CuO/AC after pre-adsorption in HCl at 120 °C. Fig. 14 displays the  $\text{Hg}^0$  removal species after pre-adsorption in 15 ppm HCl regardless of the presence of  $\text{O}_2$ . The peaks after pre-adsorption in HCl and  $\text{O}_2$  were observed at approximately 10 °C higher than the HCl-containing atmosphere, but the peak shape was extremely similar. As for the desorption characteristics of  $\text{HgCl}_x$ , it had been reported that  $\text{Hg}_2\text{Cl}_2$  decomposition occurred in two steps, while  $\text{HgCl}_2$  decomposition occurred at a single peak.<sup>44</sup> Therefore,  $\text{HgCl}_2$  is the most plausible product formed after pre-adsorption in HCl, regardless of the presence of  $\text{O}_2$ . The peak shift should be attributed to the difference in bonding sites or molecular configuration between the  $\text{Hg}-\text{Cu}-\text{Cl}-\text{O}$  system on account of the  $\text{O}_2$  atmosphere.

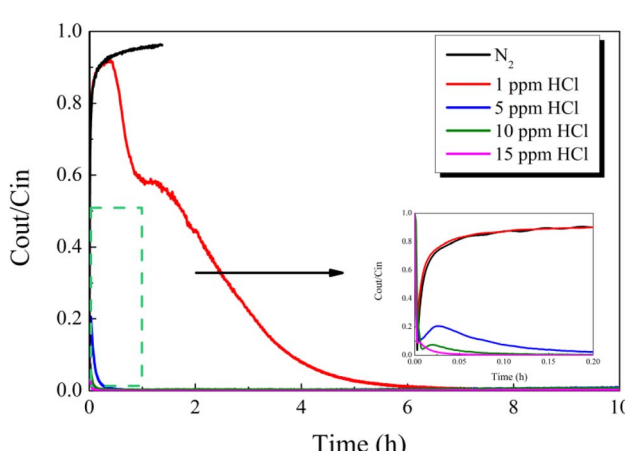


Fig. 13 Effect of HCl concentration balanced in  $\text{N}_2$  on  $\text{Hg}^0$  removal over the 12% CuO/AC catalyst at 120 °C.

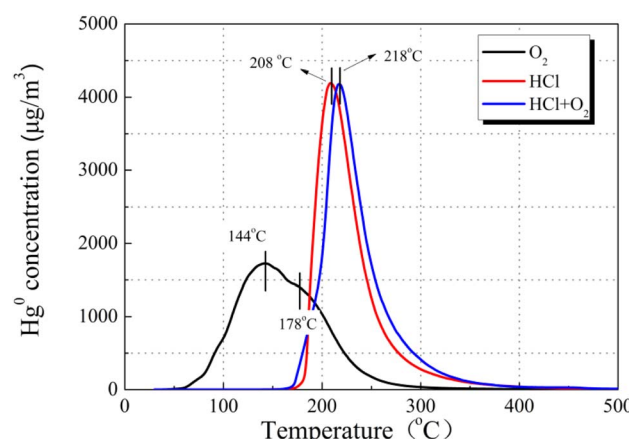


Fig. 14  $\text{Hg}^0$ -TPD patterns of the 12% CuO/AC catalyst after pre-adsorption in HCl at 120 °C (pre-adsorption reaction conditions: 15 ppm of HCl, 7%  $\text{O}_2$ , and  $\text{N}_2$  as the balance).

### 3.3. Distribution laws toward mercury removal species and proposed reaction mechanism

To comprehensively gain insights into the different flue gas components on distribution laws toward  $\text{Hg}^0$  product species, the cumulative  $\text{Hg}^0$  adsorption and oxidation efficiency was qualitatively calculated, and the results are shown in Fig. 15. As depicted, HCl was confirmed as the most effectual flue gas component contributing for  $\text{Hg}^0$  removal, and the removal efficiency almost reached 100%.  $\text{O}_2$  enhances  $\text{Hg}^0$  adsorption by 38% compared to the  $\text{N}_2$  atmosphere, while  $\text{SO}_2$  and  $\text{O}_2$  decrease  $\text{Hg}^0$  adsorption by 24% compared to pure  $\text{O}_2$ . Under the coexistence of NO and  $\text{O}_2$  atmospheres, 93% of  $\text{Hg}^0$  was captured, showing the most outstanding enhancement in terms of  $\text{Hg}^0$  adsorption, whereas the HCl atmosphere affords the most excellent enhancement by 29% for  $\text{Hg}^0$  catalytic oxidation activity. The enhancement in cumulative  $\text{Hg}^0$  removal efficiency under various flue gas components is sequenced:  $\text{O}_2 < \text{NO} < \text{HCl}$ , but this sequence is inversely proportional to their gas

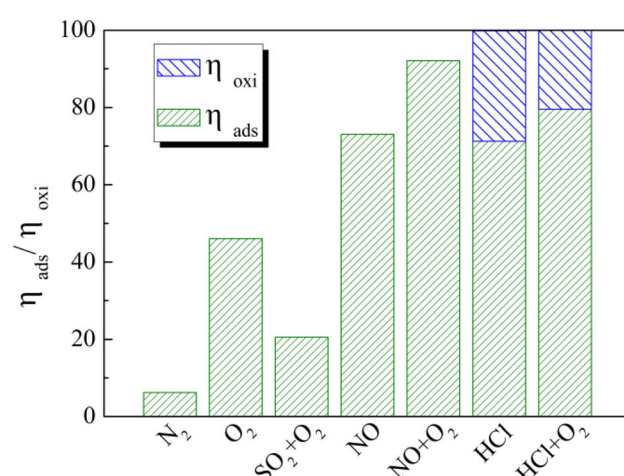


Fig. 15 Effect of individual flue gas components on  $\text{Hg}^0$  adsorption and oxidation over the 12% CuO/AC catalyst at 120 °C.

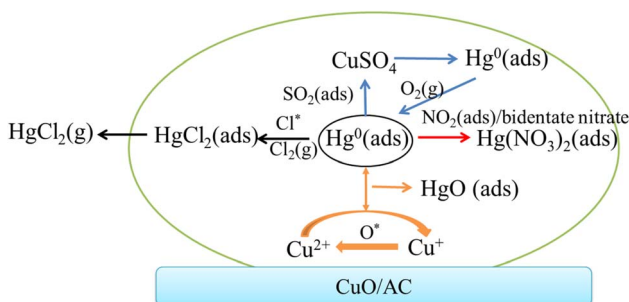


Fig. 16 Proposed removal mechanism toward  $\text{Hg}^0$  under various simulated flue gases over CuO/AC.

concentration. As a result, we assume that the affinity ability rather than the gas concentration determines the removal activities toward  $\text{Hg}^0$ , which follows the same trend as that of the cumulative  $\text{Hg}^0$  removal efficiency. This conclusion can be employed as a reference for adjusting the proportion of flue gas components to increase the removal selectivity toward  $\text{Hg}^0$ , further to improve the adsorption efficiency or the catalytic oxidation efficiency oriently.

Generally, the  $\text{Hg}^0$  removal over the CuO/AC catalyst results from a combination of physisorption, chemisorption, and catalytic oxidation. The detailed  $\text{Hg}^0$  removal mechanisms under various flue gases over the CuO/ACs catalyst are presented in Fig. 16.

First, the gaseous  $\text{Hg}^0$  physically adsorbs onto the O-terminated CuO (110) crystal planes and chemically bonds onto the Cu-terminated highly dispersed, clustered and bulk CuO surface. Then, it reacts with chemisorbed oxygen to form  $\text{HgO}$  following the Mars–Maessen mechanism.

The presence of  $\text{O}_2$  enhances both the chemisorption at the  $\text{O}_\beta$  sites and physisorption toward  $\text{Hg}^0$  and the reaction is principally controlled by chemisorption through the generation of  $\text{HgO}$ . The competitive interaction between  $\text{Hg}^0$  and  $\text{SO}_2$ , as well as the deactivation of cation vacancies of CuO leads to an inhibition in  $\text{Hg}^0$  removal, whereas the presence of  $\text{O}_2$  could weaken the damage by compensating the physically adsorbed mercury product species. In the presence of NO, the oxidizing  $\text{NO}_2$  species and/or bidentate nitrate species formed on the metal oxide and carbon matrix are favorable for  $\text{Hg}^0$  adsorption to produce  $\text{Hg}(\text{NO}_3)_2$ . In the presence of HCl, the generation of  $\text{HgCl}_2$  over the CuO/ACs catalyst involves  $\text{HOCl}$  or  $\text{Cl}_2$  oxidizing  $\text{Hg}^0$ , and a small branch of that of  $\text{HgCl}_2$  further escapes into the gas phase. The addition of the  $\text{O}_2$  atmosphere to the HCl-containing gas causes a decrease in the  $\text{Hg}^0$  oxidation efficiency.

## 4. Conclusions

CuO/ACs were prepared to remove  $\text{Hg}^0$  at lower temperatures. It was found that 12% CuO/AC exhibits higher activity toward  $\text{Hg}^0$  at 120 °C. Characterization techniques and bench-scale experiments were performed to gain insights into the structure-activity relationships, product species distribution law and the mechanism of impact of multi-component flue gases on  $\text{Hg}^0$

adsorption and oxidation over the CuO/ACs. The main conclusions from this experimental study are summarised as follows:

- $\text{Hg}^0$  removal under a  $\text{N}_2$  atmosphere over CuO/ACs is dominated by both physisorption and chemisorption, and it occurs primarily through chemisorption.
- Micropores centered at 1 nm facilitate the  $\text{Hg}^0$  physisorption. The active component of the O-terminated CuO (110) crystal planes can physically adsorb  $\text{Hg}^0$  and can chemically adsorb  $\text{Hg}^0$  through the Mars–Maessen mechanism.
- The presence of  $\text{O}_2$  enhances both physisorption and chemisorption of mercury by 38%, and the chemisorption occurring at the  $\text{O}_\beta$  sites preponderates with the product of  $\text{HgO}$ .
- Competitive adsorption and the deactivation of cation vacancies of CuO contribute to the decrease in  $\text{Hg}^0$  removal by  $\text{SO}_2$ , whereas  $\text{O}_2$  can weaken the deactivation by augmenting 20% of physically adsorbed mercury.
- NO and  $\text{O}_2$  make for the  $\text{Hg}^0$  chemisorption due to the generation of the  $\text{NO}_2$  and/or bidentate nitrate species on the metal oxide or carbon matrix, and the removal efficiency reached 93%.
- The  $\text{Hg}^0$  catalytic oxidation appears when HCl is converted into  $\text{HOCl}$  and/or  $\text{Cl}_2$ , but the catalytic oxidation efficiency of  $\text{Hg}^0$  decreases in the presence of  $\text{O}_2$  by 8%.
- The affinity abilities between various flue gases and  $\text{Hg}^0$  are in the following order:  $\text{O}_2 < \text{NO} < \text{HCl}$ .

In future studies, it is recommended that quantum chemistry methods based on density functional theory (DFT) calculations be used to simulate the reaction progress further to identify the adsorption products under multi-component flue gases and clarify the interaction mechanism in heterogeneous systems. This suggestion will be addressed in the next work.

## Data availability

The data that support the findings of this study are available from the corresponding author, Haixin Guo, upon reasonable request.

## Conflicts of interest

There are no conflicts to declare.

## Acknowledgements

This work is supported by the National Natural Science Foundation of China (No. 21607009), the Science and Technology Research and Development Program for Handan City (2342071019) the Financial Program of BJAST (24CB001-13) and the IUSE Budding Talent Program (DQ-RCB-230432).

## References

- 1 L. Tong, W. Q. Xu, Y. Yang, R. H. Liu, Y. H. Wu and T. Y. Zhu, *RSC Adv.*, 2016, **6**, 78743–78749.
- 2 R. L. Hao, X. H. Dong, Z. Wang, L. Fu, Y. Han, B. Yuan, Y. P. Gong and Y. Zhao, *Environ. Sci. Technol.*, 2019, **53**, 8324–8332.



3 H. T. Zhao, X. Luo, J. He, C. Peng and T. Wu, *Fuel*, 2015, **147**, 67–75.

4 B. A. Dranga, L. Lazar and H. Koeser, *Catalysts*, 2012, **2**, 139–170.

5 R. L. Hao, Z. Wang, Y. P. Gong, Z. Ma, Z. Qian, Y. C. Luo, B. Yuan and Y. Zhao, *J. Hazard. Mater.*, 2020, **383**, 121135.

6 H. Zhao, C. I. Ezeh, S. Yin, Z. Xie, C. H. Pang, C. Zheng, X. Gao and T. Wu, *Appl. Catal., B*, 2020, **263**, 117829.

7 W. Xu, J. Pan, B. Fan and Y. Liu, *J. Cleaner Prod.*, 2019, **216**, 277–287.

8 Z. Q. Tan, J. Xiang, S. Su, H. C. Zeng, C. S. Zhou, L. S. Sun, S. Hu and J. R. Qiu, *J. Hazard. Mater.*, 2012, **239**, 160–166.

9 Y. Ma, B. Mu, X. Zhang, D. Yuan, C. Ma, H. Xu, Z. Qu and S. Fang, *Chem. Eng. J.*, 2019, **358**, 1499–1506.

10 B. Shen, S. Zhu, X. Zhang, G. Chi, D. Patel, M. Si and C. Wu, *Fuel*, 2018, **224**, 241–249.

11 W. Q. Xu, H. R. Wang, X. Zhou and T. Y. Zhu, *Chem. Eng. J.*, 2014, **243**, 380–385.

12 M. A. Fayad, A. M. Abed, S. H. Omran, A. A. Jaber, A. A. Radhi, H. A. Dhahad, M. T. Chaichan and T. Yusaf, *Int. J. Renewable Energy Dev.*, 2022, **11**, 1068–1077.

13 M. A. Fayad, S. I. Ibrahim, S. H. Omran, F. J. Martos, T. Badawy, A. M. Al Jubori d, H. A. Dhahad and M. T. Chaichan, *Fuel*, 2023, **331**, 125549.

14 Z. Zhang, J. Liu, Z. Wang and Y. J. Yang, *Fuel*, 2021, **289**, 119791.

15 D. J. Liu, C. Lu and J. Wu, *J. Nanopart. Res.*, 2018, **20**, 277.

16 B. Zhao, H. Yi, X. Tang, Q. Li, D. Liu and F. Gao, *Chem. Eng. J.*, 2016, **286**, 585–593.

17 Y. Xiao, D. Pudasainee, R. Gupta, Z. H. Xu and Y. F. Diao, *J. Hazard. Mater.*, 2017, **336**, 232–239.

18 H. Y. Wu, C. T. Li, L. K. Zhao, J. Zhang, G. M. Zeng, Y. e. Xie, X. N. Zhang and Y. Wang, *Energy Fuels*, 2015, **29**, 6747–6757.

19 H. L. Li, C. Y. Wu, Y. Li, L. Q. Li, Y. C. Zhao and J. Y. Zhang, *J. Hazard. Mater.*, 2012, **243**, 117–123.

20 K. L. Zhao, C. T. Li, S. H. Li, Y. Wang, J. Y. Zhang, T. Wang and G. M. Zeng, *Appl. Catal., B*, 2016, **198**, 420–430.

21 L. Tong, T. Yue, P. Zuo, X. Zhang, C. Wang, J. Gao and K. Wang, *Fuel*, 2017, **197**, 1–7.

22 Y. Wu, W. Xu, Y. Yang, J. Wang and T. Zhu, *Catal. Sci. Technol.*, 2018, **8**, 297–306.

23 D. Li, X. Tang, H. Yi, D. Ma and F. Gao, *Ind. Eng. Chem. Res.*, 2015, **54**, 9097–9103.

24 B. Zhao, H. Yi, X. Tang, Q. Li, D. Liu and F. Gao, *J. Hazard. Mater.*, 2019, **364**, 700–709.

25 W. Du, L. Yin, Y. Zhuo, Q. Xu, L. Zhang and C. Chen, *Fuel Process. Technol.*, 2015, **131**, 403–408.

26 M. Trépanier, A. Tavasoli, A. K. Dalai and N. Abatzoglou, *Appl. Catal., A*, 2009, **353**, 193–202.

27 L. K. Herrera, A. Justo and J. L. Perez-Rodriguez, *J. Nano Res.*, 2009, **8**, 99–107.

28 G. Q. Zhang, Z. Li, H. Y. Zheng, T. J. Fu, Y. B. Ju and Y. C. Wang, *Appl. Catal., B*, 2015, **179**, 95–105.

29 C. Liu, S. L. Nauert, M. A. Alsina, D. Wang, A. Grant, K. He, E. Weitz, M. Nolan, K. A. Gray and J. M. Notestein, *Appl. Catal., B*, 2019, **255**, 117754.

30 A. Kubacka, M. J. Munoz-Batista, M. Fernandez-Garcia, S. Obregon and G. Colon, *Appl. Catal., B*, 2015, **163**, 214–222.

31 L. Gao, C. Li, S. Li, W. Zhang, X. Du, L. Huang, Y. Zhu, Y. Zhai and G. Zeng, *Chem. Eng. J.*, 2019, **371**, 781–795.

32 T. Boningari, P. R. Ettireddy, A. Somogyvari, Y. Liu, A. Vorontsov, C. A. McDonald and P. G. Smirniotis, *J. Catal.*, 2015, **325**, 145–155.

33 L. Tang, C. Li, L. Zhao, L. Gao, X. Du, J. Zeng, J. Zhang and G. Zeng, *Fuel*, 2018, **218**, 366–374.

34 S. H. Qiao, J. Chen, J. F. Li, Z. Qu, P. Liu, N. Q. Yan and J. Q. Jia, *Ind. Eng. Chem. Res.*, 2009, **48**, 3317–3322.

35 W. Xiang, J. Liu, M. Chang and C. Zheng, *Chem. Eng. J.*, 2012, **200–202**, 91–96.

36 H. B. Fu, X. Wang, H. B. Wu, Y. Yin and J. M. Chen, *J. Phys. Chem. C*, 2007, **111**, 6077–6085.

37 M. A. Lopez-Anton, R. Perry, P. Abad-Valle, M. Diaz-Somoano, M. R. Martinez-Tarazona and M. M. Maroto-Valer, *Fuel Process. Technol.*, 2011, **92**, 707–711.

38 S. J. Yang, Y. W. Fu, Y. Liao, S. C. Xiong, Z. Qu, N. Q. Yan and J. H. Li, *Catal. Sci. Technol.*, 2014, **4**, 224–232.

39 L. Tong, W. Q. Xu, X. Zhou, R. H. Liu and T. Y. Zhu, *Energy Fuels*, 2015, **29**, 5231–5236.

40 Y. Yang, W. Xu, J. Wang and T. Zhu, *Fuel*, 2019, **249**, 178–187.

41 M. Rumayor, M. Diaz-Somoano, M. A. Lopez-Anton and M. R. Martinez-Tarazona, *Talanta*, 2013, **114**, 318–322.

42 A. Murakami, M. A. Uddin, R. Ochiai, E. Sasaoka and S. Wu, *Energy Fuels*, 2010, **24**, 4241–4249.

43 W. M. Chen, Y. Pei, W. J. Huang, Z. Qu, X. F. Hu and N. Q. Yan, *Environ. Sci. Technol.*, 2016, **50**, 2564–2572.

44 M. A. Lopez-Anton, Y. Yuan, R. Perry and M. M. Maroto-Valer, *Fuel*, 2010, **89**, 629–634.

